



## Research Paper

## Cobalt manganese spinel as an effective cocatalyst for photocatalytic water oxidation

Linzhu Zhang, Can Yang, Zilai Xie, Xinchun Wang\*,<sup>1</sup>

State Key Laboratory of Photocatalysis on Energy and Environment, College of Chemistry, Fuzhou University, Fuzhou 350002, PR China

## ARTICLE INFO

## Keywords:

Carbon nitride

Cobalt manganese spinel

Photocatalytic water oxidation

## ABSTRACT

Efficient co-catalysts are crucial for photocatalytic water oxidation towards conversion of solar energy into chemical energy. Herein, we develop a sustainable and effective water oxidation system using graphitic carbon nitride (g-C<sub>3</sub>N<sub>4</sub>) and cubic cobalt manganese spinel (c-CoMn<sub>2</sub>O<sub>4</sub>) as light transducer and water oxidation co-catalyst, respectively. The surface modified g-C<sub>3</sub>N<sub>4</sub> with c-CoMn<sub>2</sub>O<sub>4</sub> not only accelerates the interface transfer rate of charge carriers but also reduces the excessive energy barrier for O–O formation, leading to an enhanced photocatalytic activity of water oxidation. Benefiting from the well surface engineering of g-C<sub>3</sub>N<sub>4</sub>, the g-C<sub>3</sub>N<sub>4</sub>-CoMn<sub>2</sub>O<sub>4</sub> (CN-CM) composites exhibit an enhanced performance of photocatalytic water oxidation. The oxygen evolution rate (OER) of CN-CM is 4 times higher than that of pristine g-C<sub>3</sub>N<sub>4</sub>. It is a highly active in oxidation of water, with an apparent quantum yield (AQY) of ca. 1% at 380 nm with AgNO<sub>3</sub> as sacrificial agent. This improvement is mainly due to the mixed-valence Co and Mn cations contained in c-CoMn<sub>2</sub>O<sub>4</sub> spinel.

## 1. Introduction

Photocatalytic water splitting constructing by the reduction of protons to H<sub>2</sub> and oxidation of water to O<sub>2</sub> is a promising approach to convert solar energy into clean and sustainable fuels. Since the first case that Honda-Fujishima utilized the Pt-TiO<sub>2</sub> photoelectrochemical cell for photocatalysis in 1972, great advances have been made to construct efficient heterogeneous photocatalytic system [1–3]. However, the half-reaction of water oxidation is a chemist's nightmare, in that it involves complex four-electrons redox process and high activation energy for O–O bond formation [4]. Hence, the key challenge to achieve highly efficient overall water splitting is to improve the oxygen evolution rate. During the past few years, to improve the sluggish water oxidation reaction, various strategies such as doping [5], adding molecular redox shuttles [6], constructing surface heterojunctions [7] have been adopted to modify the bulk and surface properties. Among these, deposition of suitable co-catalysts on the surface of semiconductors have proven to be one of the most effective ways to improve the interface charge separation and as well as to benefit the surface redox reaction kinetics. Importantly, a proper co-catalysts deposited on the surface of host materials can serve active sites, thereby reducing the overpotential of the oxidation reaction [8–10]. Currently, the most effective co-catalysts for water oxidation reaction are Ir- and Ru-based oxides [11–13], but the high cost and low availability hinder their wide applications.

Therefore, the development of new water oxidation cocatalysts with photoenergy translator, which are economically-viable, stable, efficient, and eco-friendly, are actively pursued in the research communities.

As inspired by Mn<sub>4</sub>CaO<sub>x</sub> clusters of photosystem II in natural photosynthesis [14,15], earth-abundant first-row (3d) transition metal based materials, such as CoO<sub>x</sub> [16,17], MnO<sub>2</sub> [18], Fe<sub>2</sub>O<sub>3</sub> [19], CoP [20,21], Co(OH)<sub>2</sub> [22], have been extensively exploited for photocatalytic water oxidation recently. Particularly, Co-based cocatalysts have attracted much attention due to their excellent performance extremely for water oxidation. For instance, when cobalt ions or spinel Co<sub>3</sub>O<sub>4</sub> deposited on the surface of substrate graphitic carbon nitride, they exhibited much higher water oxidation activities than pristine samples [23,24]. Researches demonstrated that redox transformation between different chemical valence states is very important for high water oxidation performance with tunable properties [25]. Compared with common single-metal oxides, the spinels AB<sub>2</sub>O<sub>4</sub> (A,B = metal, X = chalcogen) are more attractive due to electron hopping between different valence states of metals in O-sites and will also provide necessary surface redox active metal centers for redox reaction [26–31]. Because of many special characteristics such as the number of d electrons, e<sub>g</sub> occupancy, and metal-oxygen covalency, the spinel family has been explored in the field of electrocatalysis. Chao et al. revealed that the Mn valence state in octahedral sites of spinel MnCo<sub>2</sub>O<sub>4</sub> which was

\* Corresponding author.

E-mail address: [xcwang@fzu.edu.cn](mailto:xcwang@fzu.edu.cn) (X. Wang).<sup>1</sup> <http://wanglab.fzu.edu.cn>.

inextricably linked to its electrocatalytic OER activity, the lower Mn valence state give better OER performance. They also concluded that the  $e_g$  occupancy of the active cation in the octahedral site was the activity descriptor for the OER of spinels [32]. Liang et al. developed a  $\text{MnCo}_2\text{O}_4/\text{N}$ -doped graphene hybrid material by the nucleation and growth method [33]. They suggested that the partial substitution of  $\text{Co}^{3+}$  sites by  $\text{Mn}^{3+}$  increased the activity of catalytic sites in the hybrid materials. What's more, the covalent coupling between spinel oxide nanoparticles and N-doped reduced graphene oxide sheets, leading to excellent electrochemical properties. Therefore, the rational design of N-included photocatalyst composites with  $\text{CoMn}_2\text{O}_4$  for water oxidation turn into a potential strategy, and there have been barely reported so far.

Graphitic carbon nitride ( $\text{g-C}_3\text{N}_4$ ) polymer with graphene-like structure has motivated intensive research because of its good chemical stability, sustainability, unique electronic and optical properties, which is a promising candidate for photocatalytic water splitting due to the suitable band structure [34–37]. To date, there are many researches focused on water reduction half reaction of  $\text{g-C}_3\text{N}_4$  based photocatalysts [38–41]. But, the water oxidation reports are comparatively few. The main limiting factor for water oxidation is relatively negative valence band hybridization leading to weak oxidation ability to resist the huge energy barrier for O–O band formation [35,42]. According to previous reports, the development of efficient and cost-effective water oxidation co-catalysts to accelerate sluggish kinetic process and charge separation is worth recommend strategy [43,44]. The  $\text{c-CoMn}_2\text{O}_4$  spinel contains mixed-valence Co and Mn cations that can be catalytic sites. Furthermore, the presence of multivalent 3d metals would benefit electron conduction (by hopping) and charge transfer (through redox reactions), thus favouring the photocatalytic reaction [31]. Therefore, we adopt  $\text{c-CoMn}_2\text{O}_4$  as cocatalyst to modify  $\text{g-C}_3\text{N}_4$  for photocatalytic water oxidation. Here, we investigated a series of mixed valence cobalt manganese spinel nanoparticles decorated graphitic carbon nitrides. Various characterizations have been carried out to investigate the structure, texture, morphology, and optical and electronic properties. The photocatalytic water oxidation activities of the as-prepared samples were evaluated in assay of  $\text{O}_2$  evolution in presence of electron acceptors with light irradiation. This paper aims to develop a novel material through mixed valence spinel oxide and covalent polymer for higher effective solar-driven water oxidation. This may also open new insights in the design and development of efficient mixed valence photocatalysts for  $\text{CO}_2$  reduction, water splitting, and photovoltaic cells.

## 2. Experimental

### 2.1. Chemicals

All the chemical reagents were analytical grade and used without further purification. Urea, silver nitrate, lanthanum oxide, cobalt nitrate hexahydrate [ $\text{Co}(\text{NO}_3)_2 \cdot 6\text{H}_2\text{O}$ ], ammonia solution (25 wt%) and 50% manganous nitrate solution were obtained from China Sinopharm Chemical Reagent Company.

### 2.2. Synthesis of photocatalysts

Firstly, the cubic spinel  $\text{CoMn}_2\text{O}_4$  was prepared through facile solution-based oxidation-precipitation at modest condition according to the previously reported procedure [31]. Typically, 8 ml ammonia solution (25 wt%) was first dropped into 10 ml  $0.2 \text{ mol l}^{-1}$   $\text{Co}(\text{NO}_3)_2$  solution under stirring constantly at room temperature. Then, 20 ml  $0.2 \text{ mol l}^{-1}$   $\text{Mn}(\text{NO}_3)_2$  solution was added to the mixture, which was stirred for 120 min in the air. Afterwards, the mixture was evaporated and nitrates were fully decomposed by heating at 453 K for 2 h, yielding cubic  $\text{CoMn}_2\text{O}_4$  spinel. Then, the pristine  $\text{g-C}_3\text{N}_4$  (simple named CN) sample was prepared by the one-step thermal polymerization of urea molecules reported by our group [34]. In detail, 10 g of

urea was put into a crucible with cover, and then it was annealed at 823 K for 2 h in the air. After natural cooling, finally the pale yellow powder was collected for further use. Finally, the hybrid samples were prepared by an immersed method. For a typical preparation, 1 g of as-prepared  $\text{g-C}_3\text{N}_4$  and different amounts of  $\text{c-CoMn}_2\text{O}_4$  were immersed into 20 ml water with stirring at room temperature for 30 min. Then, the mixture was stirring at 353 K to remove water. It was denoted as  $\text{CN-CM}_x$ , where  $x$  (5, 10, 20, 30) is the percentage weight content of  $\text{c-CoMn}_2\text{O}_4$  to  $\text{g-C}_3\text{N}_4$ .

### 2.3. Characterization

X-ray diffraction (XRD) measurements were collected on a Bruker D8 Advance diffractometer with  $\text{Cu K}\alpha 1$  radiation ( $\lambda = 1.5406 \text{ \AA}$ ). Fourier transformed infrared (FTIR) spectra were recorded using a Nicolet Magna 670 FTIR spectrometer. The solid-state  $^{13}\text{C}$  NMR experiments were performed on a Bruker Advance III 500 spectrometer. TEM was performed with an FEI Tencai 20 microscope. X-ray photoelectron spectroscopy (XPS) was obtained on a Thermo ESCALAB250 instrument with a monochromatized  $\text{Al K}\alpha$  line source (200 W).  $\text{N}_2$  adsorption-desorption isotherms were carried out at 77 K using Micromeritics ASAP 2010 Surface Area and Porosity Analyzer. (DRS) were measured on a Varian Cary 500 Scan UV/Vis system. Photoluminescence (PL) spectra were recorded on an Edinburgh F1/FSTCSPC 920 spectrophotometer.

### 2.4. Photoelectrochemical measurements

Electrochemical measurements were conducted with a BioLogic VSP-300 electrochemical system in a conventional three-electrode cell, using Pt plate and saturated calomel electrode (SCE) as counter electrode and reference electrode, respectively. The working electrode was made by dip-coating the catalyst slurry ( $5 \text{ mg ml}^{-1}$  in DMF) onto F-doped tin oxide (FTO) conductor glass and the active area was confined to  $0.25 \text{ cm}^2$ . The boundary of the FTO glass was protected using Scotch tape. After air-drying, the working electrode was further dried at 423 K for 2 h to improve adhesion. Then, the Scotch tape was removed, and the uncoated part of the electrode was isolated with epoxy resin. The electrolyte was  $0.2 \text{ M Na}_2\text{SO}_4$  aqueous solution without additive (pH 6.8).

### 2.5. Photocatalytic test for water oxidation

The  $\text{O}_2$  production reactions were carried out in a Pyrex top-irradiation reaction vessel connected to a glass closed gas circulation system. For each reaction, 50 mg of catalyst powder was well dispersed in an aqueous solution (100 ml) containing  $\text{AgNO}_3$  ( $0.01 \text{ M}$ ) as an electron acceptor and  $\text{La}_2\text{O}_3$  ( $0.2 \text{ g}$ ) as a pH buffer agent. The reactor was then sealed and evacuated several times to remove air completely before irradiation under a 300 W Xe lamp with a working current of  $15 \text{ A}$  (LX300F). The wavelength of the incident light was controlled by applying some appropriate long-pass cut off filters. The reaction solution was maintained at room temperature by a flow of cooling water during the reaction. The evolved gases were analyzed in situ by a gas chromatograph equipped with a thermal conductive detector (TCD) and a  $5 \text{ \AA}$  molecular sieve column, using argon as the carrier gas. The selectivity for oxygen evolution was calculated by using the following equation:  $S = (\text{amount of evolved } \text{O}_2) / ((\text{amount of evolved } \text{O}_2) + (\text{amount of evolved } \text{N}_2))$ .

### 2.6. The apparent quantum yield (AQY) measurements

The apparent quantum yield (AQY) for the water oxidation was determined by replacing the Xe lamp with LEDs equipped with band-pass filters. The irradiation area was controlled as  $3 \times 3 \text{ cm}^2$ . The total intensity irradiation was measured by averaging 10 points in the

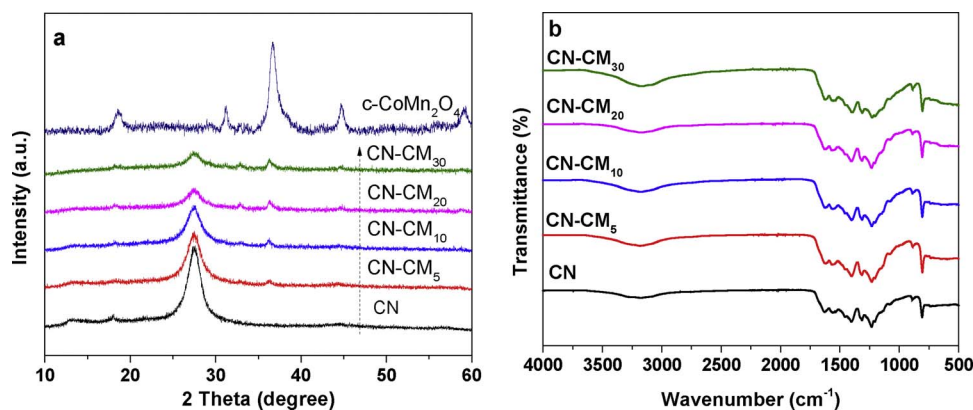


Fig. 1. (a) XRD patterns and (b) FTIR spectra of CN and CN-CM<sub>x</sub> samples.

irradiation area. For example, the average intensity was  $7.9 \text{ mW cm}^{-2}$  for the 380 nm monochromatic light (ILT 950 spectroradiometer). The AQY was calculated as follow:

$$\text{AQY\%} = N_e/N_p \times 100\% = 4 M N_A h c / S P t \lambda \times 100\%$$

Where  $N_e$  is the amount of reaction electrons,  $N_p$  is the incident photons,  $M$  is the amount of O<sub>2</sub> molecules,  $N_A$  is Avogadro's constant,  $h$  is the Plank constant,  $c$  is the speed of light,  $S$  is the irradiation area,  $P$  is the intensity of the irradiation,  $t$  is the photoreaction time, and  $\lambda$  is the wavelength of the monochromatic light.

### 3. Results and discussion

#### 3.1. Characterization of the samples

Firstly, the crystal structure and phase purity of the as-prepared sample were analyzed by XRD. As shown in Fig. 1a top line, all the diffraction peaks were identified to the space group Fd-3m and consistent with the standard values of face-centered cubic CoMn<sub>2</sub>O<sub>4</sub> (JCPDS: 23-1237). Both the CN and CN-CM<sub>x</sub> show two characteristic peaks at 13.0° and 27.4°, which can be assigned to the (100) and (002) crystal planes of CN, representing in-plane packing and interfacial stacking of CN sheets, respectively. Obviously, with the increase of the spinel loading content, the characteristic peaks of the CoMn<sub>2</sub>O<sub>4</sub> spinel were pronounced in the CN-CM<sub>x</sub>, while the two characteristic peaks intensity of CN obviously decreases. The main reason is that the order of the carbon nitride structure decreases because of the CoMn<sub>2</sub>O<sub>4</sub> load, which is consistent with earlier reports [23]. This result illustrates the successful incorporation of the c-CoMn<sub>2</sub>O<sub>4</sub> within the surface of the CN semiconductor. The FTIR spectra (Fig. 1b) of CN and CN-CM<sub>x</sub> exhibit typical breathing and stretching vibration modes of aromatic CN heterocycles and heptazine units at 1200–1600 cm<sup>-1</sup> and 810 cm<sup>-1</sup>, respectively. The broad peaks between 3000 and 3600 cm<sup>-1</sup> is attributed to the adsorbed H<sub>2</sub>O molecules and surface uncondensed amine groups vibration. The FTIR spectra illustrates the structure of modified CN did not change evidently compare with pure CN.

Structural details of the c-CoMn<sub>2</sub>O<sub>4</sub> modified carbon nitride were obtained with Solid State <sup>13</sup>C CP-MAS NMR experiment (Fig. 2). The spectra of CN-CM<sub>10</sub> and CN samples show two distinct peaks at  $\delta = 164.5$  and 156.6 ppm. The first resonance is assigned to the C (e) atoms (CN<sub>2</sub> (NH<sub>x</sub>)), whereas the second one is attributed to the C (i) atoms of melem (CN<sub>3</sub>). These signals not only confirm the existence of heptazine units and poly(tri-s-triazine) structure in CN-CM<sub>10</sub> but also show that the loading of the c-CoMn<sub>2</sub>O<sub>4</sub> don't change the structure of CN, which are in good agreement with FTIR analysis.

TEM measurements were conducted to examine the morphology of the hybrid materials. As displayed in Fig. 3a and Fig. 1S, the most of c-CoMn<sub>2</sub>O<sub>4</sub> particles with the size of 35–55 nm randomly distribute on graphitic carbon nitride surface with firm attachment, the aggregated

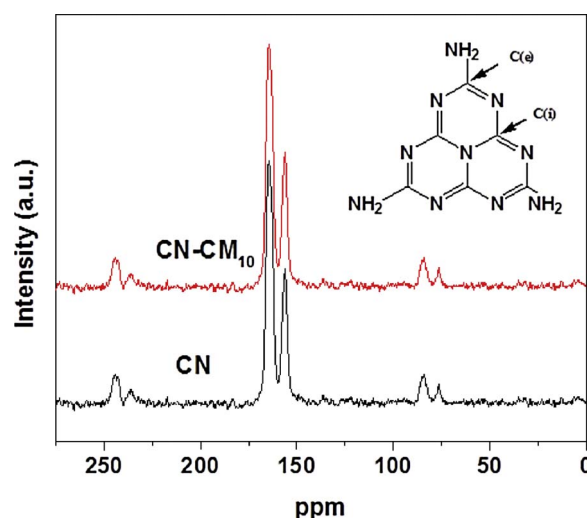


Fig. 2. The Solid state <sup>13</sup>C NMR of pure CN and CN-CM<sub>10</sub>.

particles are composed of small nanocrystals. Additionally, high-resolution TEM (HR-TEM) was also obtained to further investigate the intrinsic structure of the hybrid materials. The HR-TEM image of CN-CM<sub>10</sub>, as shown in Fig. 3b, exhibits three kinds of lattice fringes with interplanar distance of 0.28, 0.26 and 0.24 nm, which correspond to the (220), (131) and (222) atomic planes of cubic CoMn<sub>2</sub>O<sub>4</sub> structure, which agree with the XRD analysis. It is again demonstrates that we had successfully synthesized the complex of c-CoMn<sub>2</sub>O<sub>4</sub> and g-C<sub>3</sub>N<sub>4</sub> with close contact. Besides, the elemental composition of the CN-CM<sub>10</sub> was observed by energy dispersive X-ray (EDX) measurement. As shown in Fig. S2, the Co/Mn ratio is ~0.5 in the hybrid, close to the designed ratio of the c-CoMn<sub>2</sub>O<sub>4</sub>. To gain an insight into the elemental distribution of the CN-CM<sub>10</sub>, we analysed the corresponding EDX-mapping images, In Fig. 3c the elemental mapping of Co, Mn, O, C and N is clearly presented for CN-CM<sub>10</sub>, once again confirming the distribution of the CoMn<sub>2</sub>O<sub>4</sub> on the interface of CN that intends to promote the photocatalytic performance.

In order to examine the surface chemical composition and chemical states of elements in the as-prepared c-CoMn<sub>2</sub>O<sub>4</sub> and CN-CM<sub>10</sub> sample, XPS measurements were performed (Fig. 3S and Fig. 4). As shown in Fig. 4a, the survey spectra of CN-CM<sub>10</sub> only contains elemental peaks of C, N, Co, Mn, and O without other impurities. In Fig. 4b, the C1s spectrum is resolved into two peaks located at 288.1 eV and 284.6 eV, which are assigned to sp<sup>2</sup>-hybridized carbon in the N-containing aromatic ring (N–C=N) and the graphitic carbon (C=C bonds), respectively. Fig. 4c presents the N 1s spectrum with four peaks at 398.9, 400.2, 401.8, 404.1 eV. The first peak is the classical peak of sp<sup>2</sup>-hybridized nitrogen in the form of C–N=C that is regarded as the main building block of the CN. While the second peak at 400.2 eV is ascribed



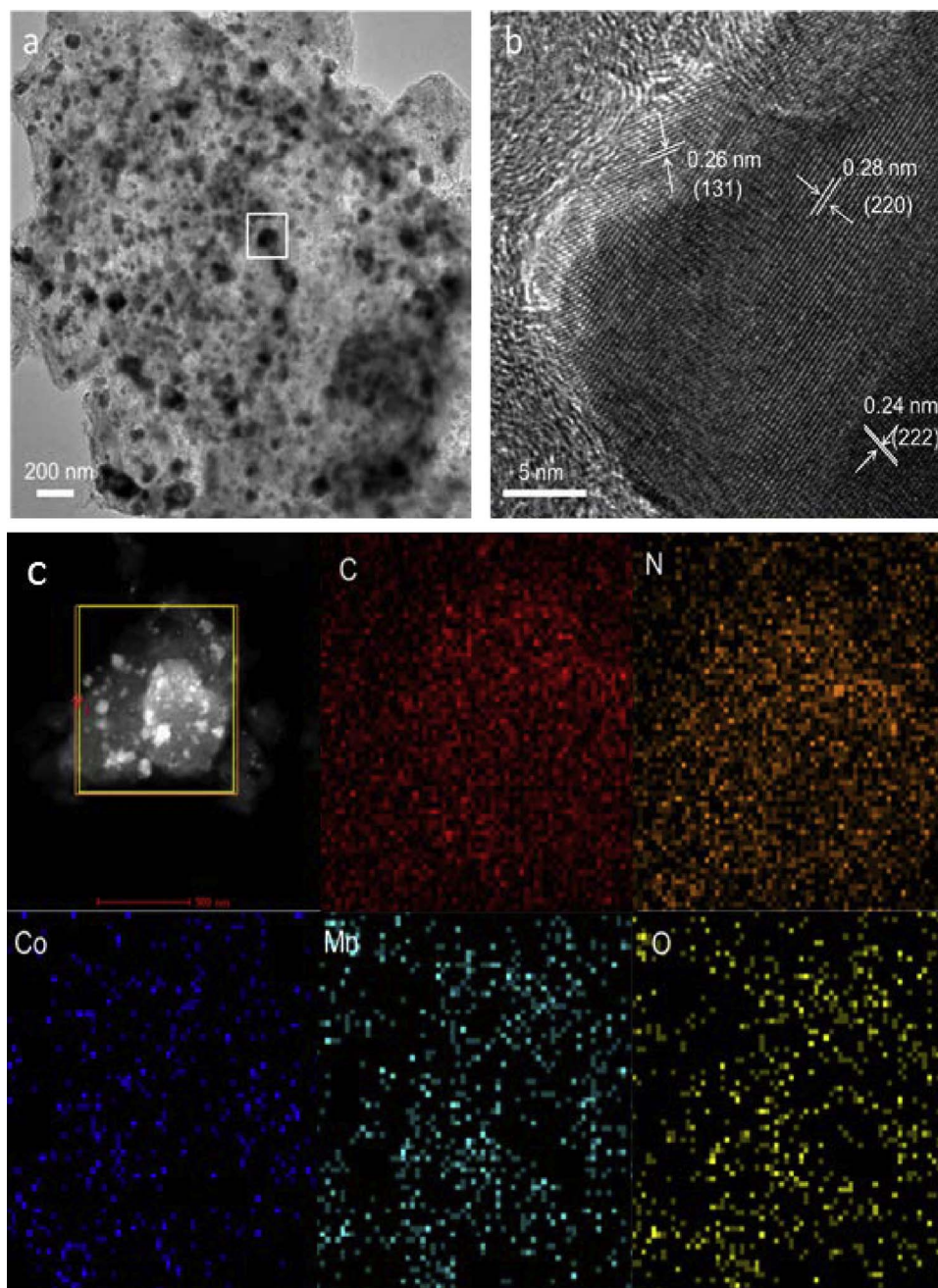


Fig. 3. (a) TEM, (b) HR-TEM, (c) elemental mapping images of the CN-CM<sub>10</sub>.

to N atoms that are bound to three C atoms are located in the heptazine ring and as bridge atom (N-C3)). Another weak peak at 401.8 eV indicated the presence of amino functional groups (C–N–H), originating from the defective condensation on heptazine substructures. Furthermore, the very weak peak at 404.1 eV is ascribed to the charging effect or positive charge localization in the heterocycles. We also carried out high-resolution of XPS analysis of Co2p. In Fig. 4d, two main peaks observed at 795.6 eV and 780.4 eV with small two satellite peaks are attributed to Co2p<sub>1/2</sub> and Co2p<sub>3/2</sub>, respectively. Generally, the energy gap between the main peaks and the satellite peaks of Co2p is very important in determining the oxidation state of cobalt. The results show that the energy gap between the Co2p<sub>1/2</sub> and Co2p<sub>3/2</sub> is about 15.2 eV, which proves that the CN-CM<sub>10</sub> possess Co<sup>2+</sup> and Co<sup>3+</sup> valence states. It is well known that high valence Co is considered to be the active sites for OER [45], this may be one of reasons for the increased catalytic activity of CN-CM<sub>10</sub>. Similarly, the Mn2p high-resolution spectrum (Fig. 4e), two main spin-orbit peaks of 2p<sub>3/2</sub> centered at ~642.1 eV and

2p<sub>1/2</sub> at ~653.5 eV, by refined fitting, the spectrum of the hybrid can be assigned to the coexistence of Mn<sup>3+</sup> and Mn<sup>4+</sup>. Compare with pure c-CoMn<sub>2</sub>O<sub>4</sub> (Fig. 3S), it is not difficult to note that the binding energy of Co and Mn is higher in the value owing to the electron cloud reduction around Co and Mn. This again illustrates the intense interaction between the c-CoMn<sub>2</sub>O<sub>4</sub> and g-C<sub>3</sub>N<sub>4</sub> with rich nitrogen lone-pair [46], which may facilitate the separation of photogenerated charge and hole, thus improving the activity of water oxidation. The O 1s spectrum in Fig. 4f could be divided into two photoelectron peaks at 530.2 eV and 531.5 eV. The first peak belongs to lattice oxygen in the spinel structure, whereas the latter peak is a typical signal of the adsorbed oxygen-containing hydroxide ions or water. All in all, the results of the XPS measurements further indicate the incorporation of c-CoMn<sub>2</sub>O<sub>4</sub> spinel on the substrate material. At the same time, the result of experiment identifies the copresence of the solid-state redox couples Co<sup>2+</sup>/Co<sup>3+</sup> and Mn<sup>3+</sup>/Mn<sup>4+</sup> in the CN-CM<sub>10</sub> sample, which may vest it with numerous redox activities for heterogeneous photocatalysis and catalysis.

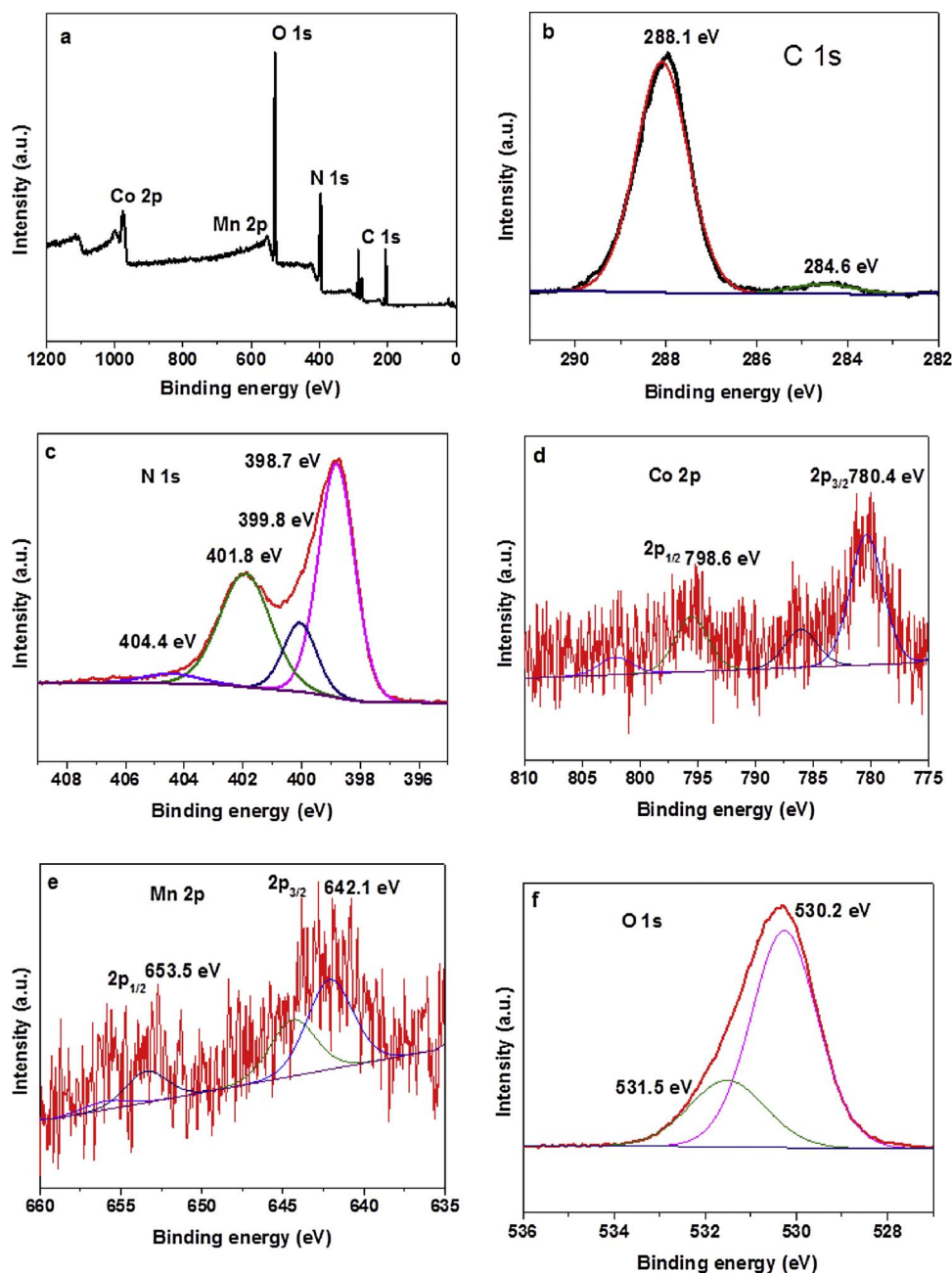


Fig. 4. XPS spectra of the CN-CM<sub>10</sub>: (a) survey spectrum and high-resolution spectra of (b) C1s, (c) N1s, (d) Co2p, (e) Mn2p and (f) O1s.

Typical N<sub>2</sub> adsorption/desorption isotherms was carried out at 77 K to analyse the surface properties of the samples. According to the IUPAC classification, Fig. 5 exhibits a type IV behavior with an H1 type hysteresis loop of samples. The BET surface areas are ca. 39 m<sup>2</sup> g<sup>-1</sup> for CN and 42 m<sup>2</sup> g<sup>-1</sup> for CN-CM<sub>10</sub>. The corresponding pore size distribution plot (Fig. 5, inset) reveals that both the CN and CN-CM<sub>10</sub> possess an average pore diameter of ~4 nm. The mesoporous characteristic formation of the materials is due to the fact that gases are released during high temperature synthesis of g-C<sub>3</sub>N<sub>4</sub>. The results show that the BET surface area of the modified carbon nitride increases a little, while the structure did not change obviously.

The optical properties of the as-prepared samples were tested by UV–vis diffuse reflection spectra (DRS) and room-temperature photoluminescence (PL), respectively. In Fig. 6a, it is worth pointing out that there is a gradually increase of broad absorption shoulder in the UV–vis absorption spectra when increasing the c-CoMn<sub>2</sub>O<sub>4</sub> content on the CN surface. Nevertheless, very few variances arising from the inherent

band structure of the CN polymer could be seen after the decoration. This is mainly because the triazine-based graphitic structure does not change after incorporation with a certain amount of c-CoMn<sub>2</sub>O<sub>4</sub>. The same result is also revealed in the solid state <sup>13</sup>C CP-MAS NMR and FTIR discussions. The enhanced optical absorption in the visible light region of hybrids is mainly due to the loading c-CoMn<sub>2</sub>O<sub>4</sub> absorb photons and then excite the internal migration of the internal d orbitals, thus have significant absorption in the visible region. However, the excessive c-CoMn<sub>2</sub>O<sub>4</sub> loading on the substrate may not be in favor of photoredox catalysis. This hypothesis can be certified by the following photocatalytic experimental results. Fig. 6b shows the PL spectra of as-prepared catalysts using excitation light of 400 nm. Notably, all of the samples show similar peaks centered at about 450 nm, with a drastic quenching of the photoluminescence intensity as the loading content increased. This phenomenon excellently indicates that the recombination of the photogenerated electrons and holes are greatly suppressed owing to the good interaction of the spinel and CN. When CN is excited

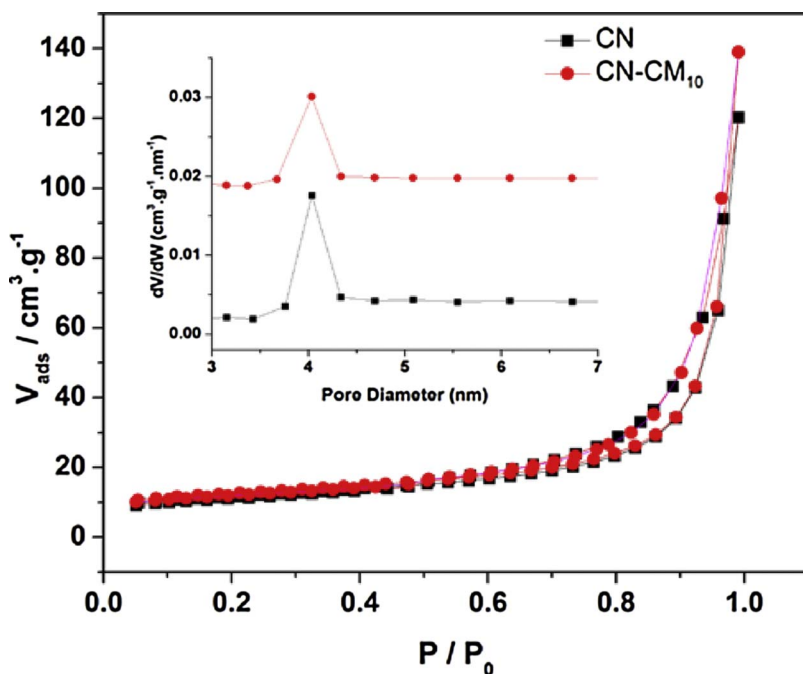


Fig. 5.  $N_2$  adsorption-desorption isotherm for samples CN and CN-CM<sub>10</sub>; insert is the corresponding BJH pore-size distribution curves.

by visible light photons, a pair of photoinduced electrons and holes are generated, which then migrate from the bulk to the interface of the semiconductor and then to the side of c-CoMn<sub>2</sub>O<sub>4</sub>, thus achieving the effective separation of electrons and holes. It is generally known that the efficient separation of photogenerated electrons and holes is one of the key factors for the enhancement of photocatalytic activity in the photocatalytic process.

Electrochemical measurements were conducted to reveal the properties of the developed c-CoMn<sub>2</sub>O<sub>4</sub>/CN hybridized material. The polarization curve (Fig. 7a) shows that the onset potential of CN-CM<sub>10</sub> is much smaller than that of CN. This is beneficial for promoting multiple-electron water oxidation kinetics and avoiding excessive driving potentials. Beyond the onset potential, a sharp rise in the photocurrent density was obtained (Fig. 7b), the current density of CN-CM<sub>10</sub> is about two-thirds times higher than that of pure CN, which strongly illustrates that the mobility of the photo-excited charge carriers is promoted. This suggests the electrical conductivity was improved at the electrode interface. Furthermore, electrochemical impedance spectroscopy (EIS) on the dark was carried out. In Fig. 7c, we can find a significantly decreased Nyquist plots diameter for CN-CM<sub>10</sub> hybrid compared with pure CN, revealing an obvious improvement in the electronic conductivity after the modification with spinel. It should be noted that all of the electrochemical experiments elucidate that the electronic conductivity of CN-CM<sub>10</sub> is obviously improved than pure CN. The main reason is

probably the intense adsorption between c-CoMn<sub>2</sub>O<sub>4</sub> and CN can provide a resistance-less path for fast charge transfer through c-CoMn<sub>2</sub>O<sub>4</sub>/CN interface. Besides, the modification of CN can provide more active sites, which decreases the overpotential for water oxidation and consequently accelerates the electrocatalytic kinetics on the CN surface.

The photocatalytic activity of the as-prepared powder samples in  $O_2$  evolution from water in the presence of the  $AgNO_3$  as an electron trapping agent was then determined. In Fig. 8, from the diagram we can clearly see that the oxygen production rate increases dramatically after the loading of c-CoMn<sub>2</sub>O<sub>4</sub> as an effective catalyst. The photocatalytic water oxidation for  $O_2$  evolution rate presents a volcanic eruption plot when varied the c-CoMn<sub>2</sub>O<sub>4</sub> content. Without loading, the pure CN shows a relatively low rate of oxygen evolution ( $\sim 4.5 \mu\text{mol h}^{-1}$ ), while a spinel loading of 5 wt% on CN results in more than twice the enhancement in activity. The optimal oxygen rate (OER) of CN-CM<sub>10</sub> is  $18.3 \mu\text{mol h}^{-1}$ , which is nearly 4-times faster than pristine CN under UV-vis irradiation ( $\lambda > 300 \text{ nm}$ ). The apparent quantum yield (AQY) of the CN-CM<sub>10</sub> oxygen evolution system was determined to be ca. 1% at 380 nm with LEDs equipped. However, further increasing the loading content reduces the activity of oxygen production, which is due to excessive loading of c-CoMn<sub>2</sub>O<sub>4</sub> on the surface of CN shielding the incident light, and thus inhibiting the light absorption and generation of photogenerated electrons and holes inside the CN. In addition, the aggregation of c-CoMn<sub>2</sub>O<sub>4</sub> also deteriorates the catalytic properties that

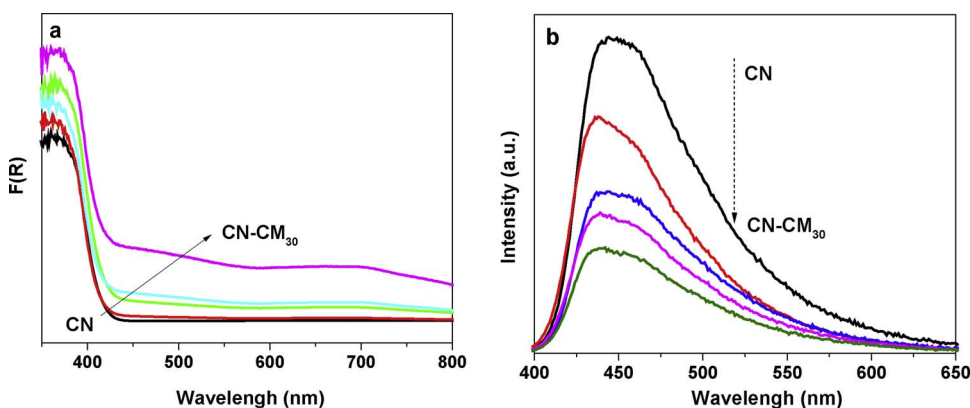


Fig. 6. UV-vis-DRS (a) and room-temperature PL (b) spectra for pure and c-CoMn<sub>2</sub>O<sub>4</sub>-modified CN sample.



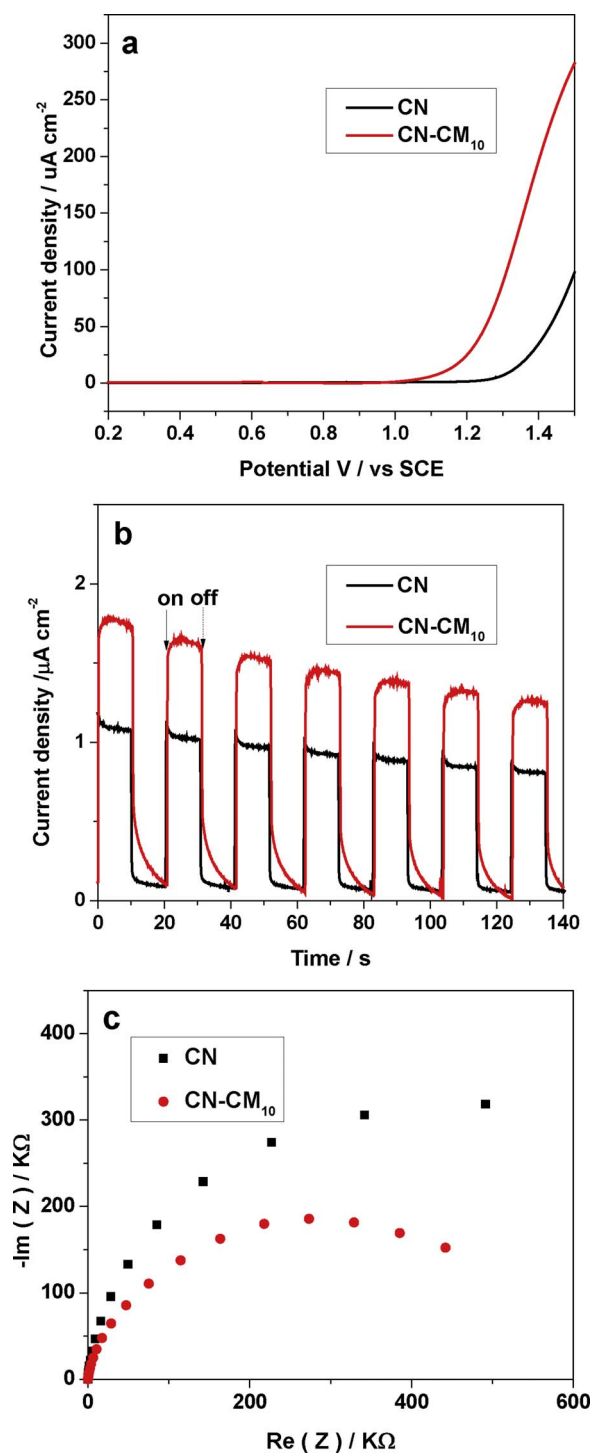


Fig. 7. (a) Polarization curves in the dark of CN and CN-CM<sub>10</sub>, (b) Transient photocurrent generation from CN and CN-CM<sub>10</sub> electrodes at 0.3 V (vs. SCE) in 0.2 M Na<sub>2</sub>SO<sub>4</sub> solution under UV-vis ( $\lambda > 300$  nm), (c) Nyquist plots of electrochemical impedance spectroscopy in the dark of CN and CN-CM<sub>10</sub> electrodes at 0.2 V vs SCE.

blocks photocatalytic water oxidation.

Moreover, long time course water oxidation experiments were measured under UV-vis irradiation. As shown in Fig. 9a, the amounts of the collected O<sub>2</sub> gases for CN-CM<sub>10</sub> is increased to 68.7  $\mu\text{mol}$ , as prolonged the reaction time to 7 h. It should be noted that rate of O<sub>2</sub> evolution decreases with increasing reaction time because of the photoreduction of Ag<sup>+</sup>, the CN-CM surface deposits more and more Ag particles that hindering light absorption and decreasing the number of samples' active sites available for reaction. This is an inevitable

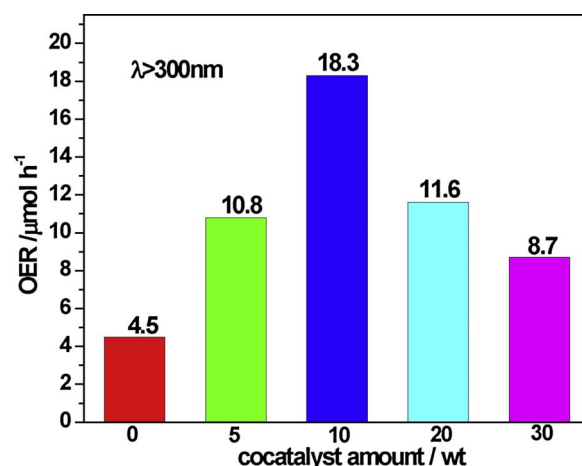


Fig. 8. OER of different amounts of c-CoMn<sub>2</sub>O<sub>4</sub> modified CN under UV-vis irradiation ( $\lambda > 300$  nm).

phenomenon in photocatalytic water oxidation based on previous reports. A low level of N<sub>2</sub> evolutions were detected in the reaction stage for both CN and CN-CM samples. This is ascribed to the photooxidation/photocorrosion of CN, more importantly, after the spinel c-CoMn<sub>2</sub>O<sub>4</sub>-modification the catalytic selectivity towards nitrogen is remarkably reduced in term of the molar ratio of N<sub>2</sub>/(N<sub>2</sub> + O<sub>2</sub>). This result once again reveals that intense interactions between CN and spinel could facilitate the hole migration from CN to the spinel. It is beneficial to the separation of electrons and holes, which promotes the production of oxygen. Besides, we have evaluated the oxygen evolution rate (OER) of the CN-CM<sub>10</sub> sample under different specific wavelength illuminations. As shown in Fig. 9b, the OER of the samples is associated with DRS spectra. When the illumination wavelengths are  $\lambda > 360$ , 380, 420, 420 and 550 nm, the values are 13, 10.3, 4.1 and 0  $\mu\text{mol h}^{-1}$ , respectively. This confirms that the photocatalytic oxygen evolution reaction is indeed a photo-induced process.

In order to further identify the role of c-CoMn<sub>2</sub>O<sub>4</sub> in the catalytic reaction, we use it to modify the inorganic semiconductor (eg. BiVO<sub>4</sub>, WO<sub>3</sub>) for photocatalytic water oxidation. As shown in Fig. 10, it can be observed that the water oxidation rate of all samples have been improved under visible light irradiation ( $\lambda > 420$  nm). According to experimental data we may be able to draw a conclusion the c-CoMn<sub>2</sub>O<sub>4</sub> can be used as an effective and universal co-catalyst for Photocatalytic water oxidation. More interestingly, the increased water oxidation rate of CN-CM<sub>10</sub> is most obvious (about three times). One hand, this phenomenon possibly owing to CN can be regarded as a good Lewis base for coordination reaction with metal ions due to the existence of rich nitrogen compare with BiVO<sub>4</sub> and WO<sub>3</sub>. The intense interaction between the host and guest materials facilitates the separation of photo-generated electrons and holes, resulting in an increase of photocatalytic oxygen evolution. On the other hand, the BiVO<sub>4</sub> and WO<sub>3</sub> are widely regarded as the most efficient materials for photocatalytic water oxidation, their water oxidation overpotential is relatively low compared to g-C<sub>3</sub>N<sub>4</sub>, so the modification of c-CoMn<sub>2</sub>O<sub>4</sub> only slightly promote their oxygen evolution rate, while the overpotential of g-C<sub>3</sub>N<sub>4</sub> photocatalytic water oxidation can be significantly reduced after the modification of c-CoMn<sub>2</sub>O<sub>4</sub>.

To further emphasize the important role of the multivalent metal spinel c-CoMn<sub>2</sub>O<sub>4</sub> for water oxidation, we also investigated the behaviors of the single-valent Co<sup>2+</sup> and Mn<sup>2+</sup> as co-catalysts for water oxidation reaction. As shown in Table 1, it is interesting observed that the addition of Co<sup>2+</sup> enhances the water oxidation rate nearly two times, while Mn<sup>2+</sup> nearly has no effect on water oxidation rate. This reveals that the mixed-valence oxides are advantageous as co-catalysts because the alternating valence states of cations can provide donor-acceptor chemisorption sites for desorption of H<sub>2</sub>O. Meanwhile, the

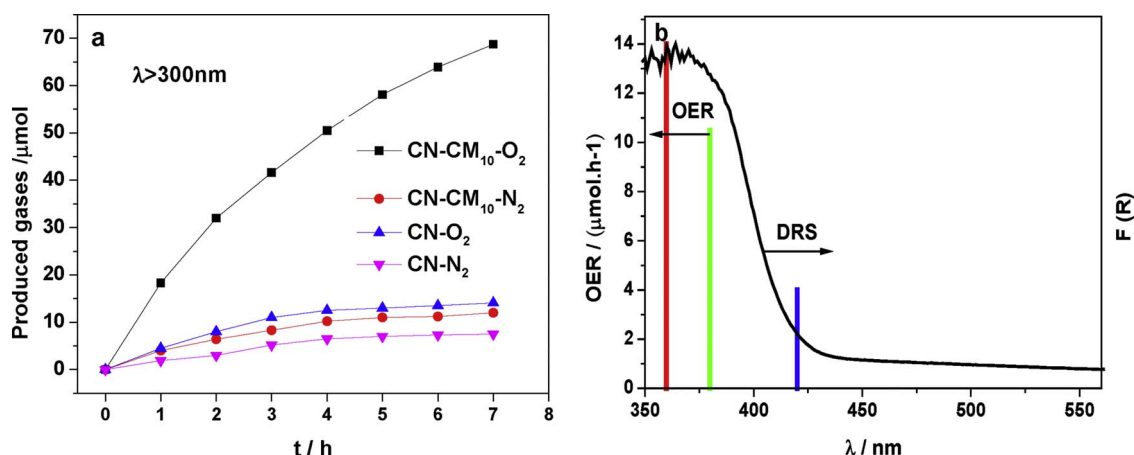


Fig. 9. (a) Time course water oxidation activities of CN and CN-CM<sub>10</sub> under UV-vis irradiation ( $\lambda > 300$  nm), (b) The OER of the c-CoMn<sub>2</sub>O<sub>4</sub> modified g-C<sub>3</sub>N<sub>4</sub> under different specific wavelength illuminations.

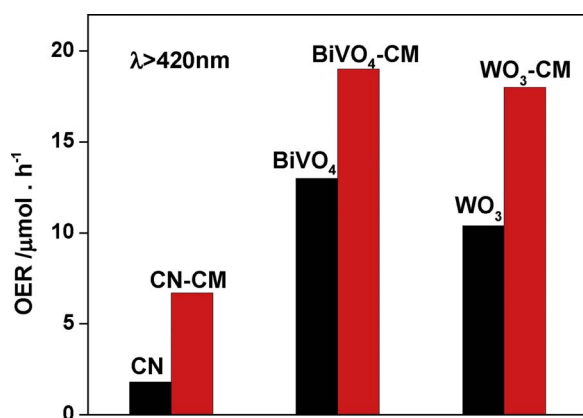


Fig. 10. OER of c-CoMn<sub>2</sub>O<sub>4</sub> modified different semiconductors under visible-vis irradiation ( $\lambda > 420$  nm).

Table 1

Co<sup>2+</sup>, Mn<sup>2+</sup> and multivalent c-CoMn<sub>2</sub>O<sub>4</sub> as cocatalyst to promote O<sub>2</sub> evolution rate of CN under light irradiation ( $\lambda > 300$  nm).

Entry	Sample	Cocatalyst	Amount of cocatalyst/wt%	O <sub>2</sub> evolution rate/ $\mu\text{mol h}^{-1}$
1	CN	–	–	4.5
2	CN	c-CoMn <sub>2</sub> O <sub>4</sub>	10	18.2
3	CN	Co(NO <sub>3</sub> ) <sub>2</sub>	10	9.5
4	CN	Mn(NO <sub>3</sub> ) <sub>2</sub>	10	4.2

synergistic effect of Co and Mn cations in spinel probably accelerates the water oxidation kinetics than single-valent Co<sup>2+</sup> and Mn<sup>2+</sup>. This experimental results further elucidate the spinels with mixed-valence are more advantageous in the process of catalytic water oxidation.

#### 4. Conclusion

In summary, we develop a facile impregnating method to fabricate CN-CM composite for photocatalytic water oxidation. The simple and cheap modification of c-CoMn<sub>2</sub>O<sub>4</sub> significantly reduces the huge energy barrier for O–O band formation, and accelerates the water oxidation kinetics. The CN-CM<sub>10</sub> composite exhibits up to 4-fold enhancement in oxygen evolution rate than that of the pristine CN under UV-vis irradiation. Our work further reveals the activity origin not only owing to the optimizing of the optical, electrical, and texture properties of hybrid materials but also offering more active sites for surface reactions. What's more, the strong mutual attraction of mixed-valence c-CoMn<sub>2</sub>O<sub>4</sub>

and g-C<sub>3</sub>N<sub>4</sub> with lots of lone pair electrons greatly promote interface charge separation and allow for the lowering of overpotential of water oxidation. It deserves to note that the particle size of c-CoMn<sub>2</sub>O<sub>4</sub> cocatalyst is relatively large at present, in the next work, we can synthesis c-CoMn<sub>2</sub>O<sub>4</sub> cocatalysts with smaller size have a larger surface and more active sites to significantly enhance photocatalytic efficiency. Meanwhile, this work may bring some insights into the target-directed design of other technologically important nanocrystalline spinel oxides such as FeCo<sub>2</sub>O<sub>4</sub>, NiCo<sub>2</sub>O<sub>4</sub>, ZnCo<sub>2</sub>O<sub>4</sub> and ZnMn<sub>2</sub>O<sub>4</sub> with sustainable substrate rich in lone electrons for practical application in future energy cycles.

#### Acknowledgement

This work was financially supported by the National Natural Science Foundation of China (21425309 and 21761132002) and the 111Project.

#### Appendix A. Supplementary data

Supplementary data associated with this article can be found, in the online version, at <http://dx.doi.org/10.1016/j.apcatb.2017.11.023>.

#### References

- [1] A. Kudo, Y. Miseki, Chem. Soc. Rev. 38 (2009) 253–278.
- [2] A. Fujishima, K. Honda, Nature 238 (1972) 37–38.
- [3] K. Maeda, K. Domen, J. Phys. Chem. Lett. 1 (2010) 2655–2661.
- [4] A.R. Parent, R.H. Crabtree, G.W. Brudvig, Chem. Soc. Rev. 42 (2013) 2247–2252.
- [5] F. Razmjooei, K.P. Singh, D.-S. Yang, W. Cui, Y.H. Jang, J.-S. Yu, ACS Catal. 7 (2017) 2381–2391.
- [6] J.X. Li, C. Ye, X.B. Li, Z.J. Li, X.W. Gao, B. Chen, C.H. Tung, L.Z. Wu, Adv. Mater. 29 (2017).
- [7] C. Li, T. Wang, Z. Luo, S. Liu, J. Gong, Small 12 (2016) 3415–3422.
- [8] J. Ran, J. Zhang, J. Yu, M. Jaroniec, S.Z. Qiao, Chem. Soc. Rev. 43 (2014) 7787–7812.
- [9] J. Yang, D. Wang, H. Han, C. Li, Acc. Chem. Res. 46 (2013) 1900–1909.
- [10] K. Maeda, A. Xiong, T. Yoshinaga, T. Ikeda, N. Sakamoto, T. Hisatomi, M. Takashima, D. Lu, M. Kanehara, T. Setoyama, T. Teranishi, K. Domen, Angew. Chem. Int. Ed. 49 (2010) 4096–4099.
- [11] B.H. Meekins, P.V. Kamat, J. Phys. Chem. Lett. 2 (2011) 2304–2310.
- [12] B. Ma, J. Yang, H. Han, J. Wang, X. Zhang, C. Li, J. Phys. Chem. C 114 (2010) 12818–12822.
- [13] J. Sato, N. Saito, Y. Yamada, K. Maeda, T. Takata, J.N. Kondo, M. Hara, H. Kobayashi, K. Domen, Y. Inoue, J. Am. Chem. Soc. 127 (2005) 4150–4151.
- [14] J. Yano, J. Kern, K. Sauer, M.J. Latimer, Y. Pushkar, J. Biesiadka, B. Loll, W. Saenger, J. Messinger, A. Zouni, V.K. Yachandra, Science 314 (2006) 821–825.
- [15] M.M. Najafpour, T. Ehrenberg, M. Wiechen, P. Kurz, Angew. Chem. Int. Ed. 49 (2010) 2233–2237.
- [16] F. Zhang, A. Yamakata, K. Maeda, Y. Moriya, T. Takata, J. Kubota, K. Teshima, S. Oishi, K. Domen, J. Am. Chem. Soc. 134 (2012) 8348–8351.
- [17] A.E. Maegli, S. Pokrant, T. Hisatomi, M. Trottmann, K. Domen, A. Weidenkaff, J. Phys. Chem. C 118 (2014) 16344–16351.



- [18] L. Liu, Z. Ji, W. Zou, X. Gu, Y. Deng, F. Gao, C. Tang, L. Dong, *ACS Catal.* 3 (2013) 2052–2061.
- [19] R.D.L. Smith, M.S. Prevot, R.D. Fagan, Z. Zhang, P.A. Sedach, M.K.J. Siu, S. Trudel, C.P. Berlinguette, *Science* 340 (2013) 60–63.
- [20] Z. Pan, Y. Zheng, F. Guo, P. Niu, X. Wang, *ChemSusChem* 10 (2017) 87–90.
- [21] J. Ryu, N. Jung, J.H. Jang, H.-J. Kim, S.J. Yoo, *ACS Catal.* 5 (2015) 4066–4074.
- [22] G. Zhang, S. Zang, X. Wang, *ACS Catal.* 5 (2015) 941–947.
- [23] G. Zhang, C. Huang, X. Wang, *Small* 11 (2015) 1215–1221.
- [24] J. Zhang, M. Grzelczak, Y. Hou, K. Maeda, K. Domen, X. Fu, M. Antonietti, X. Wang, *Chem. Sci.* 3 (2012) 443–446.
- [25] M.W. Kanan, D.G. Nocera, *Science* 321 (2008) 1072–1075.
- [26] F. Cheng, J. Shen, B. Peng, Y. Pan, Z. Tao, J. Chen, *Nat. Chem.* 3 (2011) 79–84.
- [27] C. Xiao, X. Zhang, T. Mendes, G.P. Knowles, A. Chaffee, D.R. MacFarlane, *J. Phys. Chem. C* 120 (2016) 23976–23983.
- [28] X.-F. Lu, L.-F. Gu, J.-W. Wang, J.-X. Wu, P.-Q. Liao, G.-R. Li, *Adv. Mater.* 29 (2017).
- [29] B. Cui, H. Lin, Y.-z. Li, J.-b. Li, P. Sun, X.-c. Zhao, C.-j. Liu, *J. Phys. Chem. C* 113 (2009) 14083–14087.
- [30] Y. Ren, L. Lin, J. Ma, J. Yang, J. Feng, Z. Fan, *Appl. Catal. B: Environ.* 165 (2015) 572–578.
- [31] C. Li, X. Han, F. Cheng, Y. Hu, C. Chen, J. Chen, *Nat. Commun.* 6 (2015) 7345.
- [32] C. Wei, Z. Feng, G.G. Scherer, J. Barber, Y. Shao-Horn, Z.J. Xu, *Adv. Mater.* 29 (2017).
- [33] Y. Liang, H. Wang, J. Zhou, Y. Li, J. Wang, T. Regier, H. Dai, *J. Am. Chem. Soc.* 134 (2012) 3517–3523.
- [34] X. Wang, K. Maeda, A. Thomas, K. Takanabe, G. Xin, J.M. Carlsson, K. Domen, M. Antonietti, *Nat. Mater.* 8 (2009) 76–80.
- [35] Y. Zheng, L. Lin, B. Wang, X. Wang, *Angew. Chem. Int. Ed.* 54 (2015) 12868–12884.
- [36] F.K. Kessler, Y. Zheng, D. Schwarz, C. Merschjann, W. Schnick, X. Wang, M.J. Bojdys, *Nat. Rev. Mater.* 2 (2017) 17030.
- [37] W.J. Ong, L.L. Tan, Y.H. Ng, S.T. Yong, S.P. Chai, *Chem. Rev.* 116 (2016) 7159–7329.
- [38] Z.-A. Lan, G. Zhang, X. Wang, *Appl. Catal. B: Environ.* 192 (2016) 116–125.
- [39] L. Lin, H. Ou, Y. Zhang, X. Wang, *ACS Catal.* 6 (2016) 3921–3931.
- [40] C. Yang, B. Wang, L. Zhang, L. Yin, X. Wang, *Angew. Chem. Int. Ed.* 56 (2017) 6627–6631.
- [41] G. Zhang, G. Li, Z.-A. Lan, L. Lin, A. Savateev, T. Heil, S. Zafeirotos, X. Wang, M. Antonietti, *Angew. Chem. Int. Ed.* 56 (2017) 13445–13449.
- [42] V.S. Kale, U. Sim, J. Yang, K. Jin, S.I. Chae, W.J. Chang, A.K. Sinha, H. Ha, C.-C. Hwang, J. An, H.-K. Hong, Z. Lee, K.T. Nam, T. Hyeon, *Small* 13 (2017).
- [43] L. Jiang, X. Yuan, Y. Pan, J. Liang, G. Zeng, Z. Wu, H. Wang, *Appl. Catal. B: Environ.* 217 (2017) 388–406.
- [44] T. Xiong, W.L. Cen, Y.X. Zhang, F. Dong, *ACS Catal.* 6 (2016) 2462–2472.
- [45] B. Zhang, X. Zheng, O. Voznyy, R. Comin, M. Bajdich, M. Garcia-Melchor, L. Han, J. Xu, M. Liu, L. Zheng, F.P.G. de Arquer, C.T. Dinh, F. Fan, M. Yuan, E. Yassitepe, N. Chen, T. Regier, P. Liu, Y. Li, P. De Luna, A. Janmohamed, H.L. Xin, H. Yang, A. Vojvodic, E.H. Sargent, *Science* 352 (2016) 333–337.
- [46] X. Ge, Y. Liu, F.W.T. Goh, T.S.A. Hor, Y. Zong, P. Xiao, Z. Zhang, S.H. Lim, B. Li, X. Wang, Z. Liu, *ACS Appl. Mater. Interfaces* 6 (2014) 12684–12691.